Single cell cryo-soft X-ray tomography shows that each *Chlamydia trachomatis* inclusion is a unique community of bacteria

Patrick Phillips[1,2,4], James M. Parkhurst[1,3], Ilias Kounatidis[1], Chidinma Okolo[1], Thomas M. Fish[1], James H. Naismith[2,3], Martin A. Walsh[1,2], Maria Harkiolaki[1,2], Maud Dumoux[1,2,3*]

[1] Diamond Light Source, Harwell Science and Innovation Campus, Didcot, OX11 0DE, UK

[2] Research Complex at Harwell, Harwell Science and Innovation Campus, Didcot, OX11, UK

[3] the Rosalind Franklin Institute, Fermi Road, Didcot, OX11 0FA

[4]University of Oxford, Division of Structural biology department, Roosevelt Drive, Oxford, OX3 7BN

[*]corresponding author: maud.dumoux@rfi.ac.uk

Abstract

The impact of the cell community on its individual components in the prokaryotic realm is often overlooked. However, in the case of intracellular pathogens, where each infected cell can be considered as a single community, understanding how a population adapts to its environment to evolve and successfully propagate is key. *Chlamydia* infections are characterised by a silent propagation of the bacteria within individual hosts and the wider population. *Chlamydia* are strict intracellular pathogens residing within a specialised membrane-bound compartment called the inclusion. The life cycle of *Chlamydia* involves altering between the invasive elementary bodies (EBs) and replicative reticulate bodies (RBs). We have used cryo-soft X-ray tomography to observe individual inclusions, combining excellent resolution (40 nm) and large volume imaging (up to 16 µm). Combined with a semi-automated segmentation pipeline, we were able to consider each inclusion as an individual bacterial niche. Within the inclusion, we identified and classified different forms of the bacteria and confirmed the recent finding that RBs have a variety of volumes (small, large and abnormal). Moreover, we demonstrate that the proportions of these different RB forms depend on the bacterial concentration in the cell demonstrating the impact of the group on its individual component. We conclude that each inclusion operates as an autonomous community which regulates the characteristics of individual bacteria within the inclusion.

Keywords: Chlamydia; bacteria community; cryo-soft X-ray tomography; segmentation

Introduction

Chlamydiacae are pathogenic to both humans and animals. *C. pecorum* infection impacts livestock (Borel, 2018) and wildlife including the iconic Koala[-] (Waugh, 2017). In humans, *Chlamydiae* are the primary cause of acquired blindness worldwide (Taylor, 2014) and, in developed countries, it is a leading cause of bacterial sexually transmitted disease with adverse consequences for fertility (O'Connell, 2016). *Chlamydiae* are also responsible for atypical pneumonias (Cunha, 2006) and are associated with Reiter's syndromes (Amor, 1983) and cardiovascular diseases (Boland, 2000). In this work we consider *Chlamydia trachomatis* LymphoGranuloma Venereum 2 responsible for sexually transmitted disease, outbreaks of which have been reported across the United States and Europe in men who have sex with men (Richardson, 2007).

Chlamydiae are intracellular bacteria found in two morphologically distinct forms: the elementary body (EB), the non-dividing infectious form, and the reticulate body, the dividing non-infectious form. These forms inter convert within a compartment named the inclusion. Having entered the cell, EBs convert to RBs which multiply. RBs then convert back to EBs which then break out of the cell ensuring onward propagation by infecting neighbouring cells. Therefore, during the life cycle, the bacterial inclusion forms, matures, expands and ultimately exits the cell (Elwell, 2016). Since the end point of the intracellular growth of *Chlamydiae* is the formation of an inclusion containing a large number of newly formed EBs, there is a link between the size of the inclusion and the maturation of the bacteria population (Engström, 2015). The EB and RB forms of *Chlamydiae* have a very different size (volume) (Higashi, 1965). Application of common analytical technics are very difficult as *Chlamydia* are genetically intractable (Robert J. Bastidas, 2016) and probes such as DNA intercalants or other chemicals interfere with the host cell function (Cottet-Rousselle, 2011) (Davies, 2006). Within each inclusion the bacterial community must coordinate two processes, RB replication and RB conversion to EB (Elwell, 2016). A study by Lee et al. in 2018 using serial block face electron microscopy (sbf-EM) has shed insights into the evolution of a *Chlamydia* inclusion (Lee, 2018). Sbf-TEM, although powerful, took an average of 25h per region of interest and generated up to 500 sections, each requiring manual segmentation. Moreover, sbf-EM uses fixed resin-embedded samples which are mechanically sectioned. Fixation induces 'membrane blisters' (Shelton, 1978) and damaged organelles such as mitochondria whilst dehydration can remove molecules and form vacuoles (Cheville, 2014). Sectioning can introduce sample compression, thickness variation and knife marks (Richter, 1994; Monikandan, 2016). Cryogenic soft X-ray tomography (cryo-SXT) provides the means to bypass these sample preparation induced artifacts and to image frozen hydrated chlamydia infected cells in their near native state at the 10s of nm resolution range.

Here we report the deployment of cryogenic soft X-ray tomography (cryo-SXT) to study the organisation of the *Chlamydia* inclusion at the stage where there is both active RB division and transformation into the EB form. We have used a semi-automated segmentation approach using freely available software. The data (40 nm nominal resolution, depth of focus 10 µm) demonstrate that bacterial concentration is an important factor in the regulation of the reticulate body volume.

Results

Imaging *Chlamydia* inclusion with cryo-SXT: advantages and limitations

Samples were prepared on EM grids; the use of such 2D supports is standard in cellular imaging as it allows access for manipulation (Kounatidis, 2020). Finder grids were used to allow correlative microscopy to quickly locate the inclusion. We decided to work at low infectivity with inclusion forming units (IFU) between 0.5 and 0.8 to mimic physiological infection. Cryo-SXT data were acquired at Diamond Light Source on beamline B24 which can image at 25 nm or 40 nm resolution using absorption contrast imaging. At 25 nm, images showed *Chlamydia* inclusions at 24 hpi (hours post infection) with the expected features of *Chlamydia* and host cells (Figure 1 A-D). The host cell cytoskeleton, mitochondrial cristae and the endoplasmic reticulum (ER) were clear (Figure 1 A, B and D). The bacterial inner and outer membrane and the membrane invagination typical of the PVC (*Planctomycetes, Verrucomicrobia, Chlamydiae*) super-phylum (Santarella-Mellwig, 2010) (Figure 1 A and B) were visible. We observed the characteristic accumulation of glycogen (grey amorphous globules) within the inclusion lumen (Gordon, 1965) and the characteristic type III secretion system array in contact with the ER (the 'pathogenic synapse') (Figure 1B and C) (Dumoux, 2012). This higher resolution Cryo-SXT thus confirms that this approach yields images with the expected features of the system free from distortion. In order to image a volume sufficient for an entire inclusion in a single

experiment, 40 nm resolution was used (Figure 1D). At 40 nm the inner and outer membrane were no longer distinct and the glycogen granules were less defined. However, the inclusion membrane, the mitochondria, cytoskeleton and ER remain clearly visible. At 40 nm resolution, an entire inclusion was imaged in around 40 min (Figure 1E).

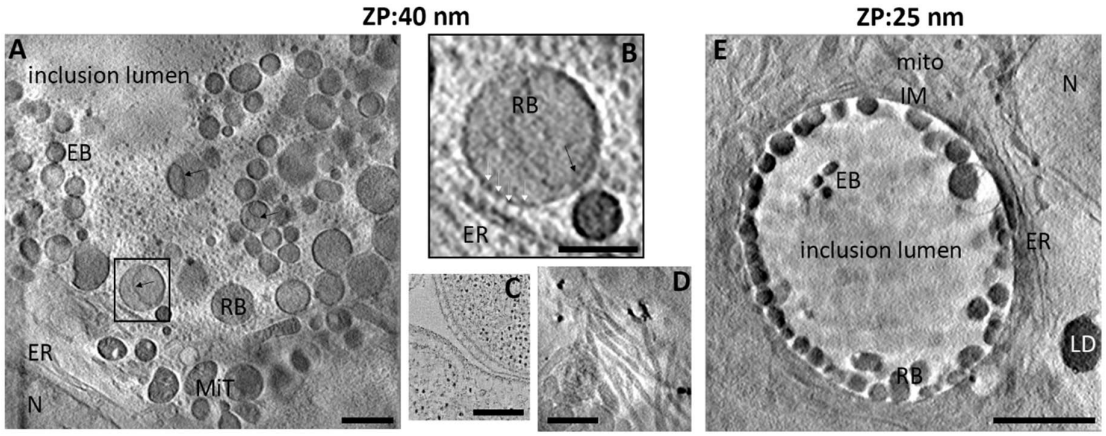

Figure 1: Observation using cryo-SXT and characterisation of HeLa cells infected by C. trachomatis. *HeLa cells infected with C. trachomatis for 24 hpi and observed using cryo-SXT using a 25 nm zone plate (A, B and D) or 40 nm (E) zone plate. MiT: mitochondria, N: nucleus, EB: elementary body, RB: reticulate, IM: inclusion membrane, ER: endoplasmic reticulum body, LD: lipid droplets black arrow: inner membrane invagination, (B) corresponds to the box in A and highlights the presence of the pathogen synapse with the T3SS array (white arrow heads), (C): from Dumoux et al (2012), TEM of the pathogen synapse for reference. D: host cell cytoskeleton. Scale bars: 1 µm(A and D) 0.5 µm (B), 250 nm (C) and 5 µm (E).*

The tomographic reconstruction was performed using the IMOD software package (Kremer, 1996). **This step consists in the alignment of the frame within the tilt series (a frame is an image at a certain angle) so after weighted back projection a stack (series of z planes) can be obtained.** The segmentation of the inclusion was completed using SuRVoS (Luengo, 2017). We then used ImageJ (Schindelin, 2012) to segment individual bacteria within the inclusion (macro detailed in supplementary material). We relied on manual curation to remove the incorrect objects and add back objects which were incorrectly fragmented. This was simplified as each object was associated with an identification number. At the end of the process, every segmented object is associated with an identification number and a volume. The entire computational process, from tomogram reconstruction to segmentation including curation took approximatively 8 h per inclusion.

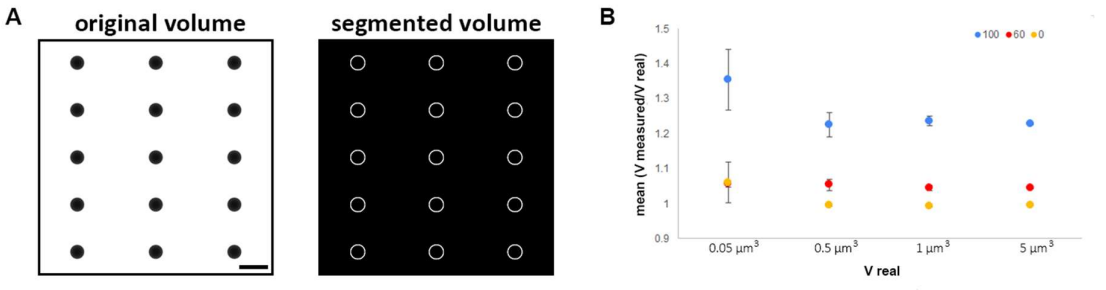

Figure 2: Impact of the missing wedge using simulation data composed of spheres of different volumes*. A) An example of segmented simulated data (0.5 µm³ spheres, 0 ° tilt) On the left, with the raw data and right the segmented volume which recognises boundaries. Scale: 1 µm. B) Mean ratio (measured volume/real volume) as a function of the real volume with different missing wedges of data (100° (blue) or 60 ° (red) or no missing wedge (yellow).*

Projection tomography is based on the Radon transform (Radon, 1917) **where a series of image of an object are acquired uniformly over 180° can be transformed into Fourier space so the object can be projected back to real space in its full volume. However, practical limitations, such as holder tilt range, sample thickness, sample carrier, often restrict the data acquisition to less than 180°.** At B24 the setup allows projection images to be recorded from -70° to +70°. The consequence of an incomplete tilt range is referred to as 'the missing wedge' (Löwe, 2014). We simulated a set of tilt series containing several spheres (0.05, 0.5, 1 and 5 μm^3) with different missing wedges (0°, 60° and 100°). The volumes were accurately calculated within 0.05% error when there was no missing wedge (Figure 2). As expected, the larger the missing wedge, the more inaccurate the volume calculations were. Smaller volumes were more severely affected than larger ones, this may also convolve segmentation errors. The presence of objects that obstruct the X-rays, such as grid bars, also remove data and this is sample specific. Our approach was to record all tilt series with a uniform missing wedge of 85° so as to have a standardized approach to the unavoidable problem of the missing wedge of data. We used our segmentation pipeline to segment and calculate the volume of every individual bacterium (event) (Figure 3).

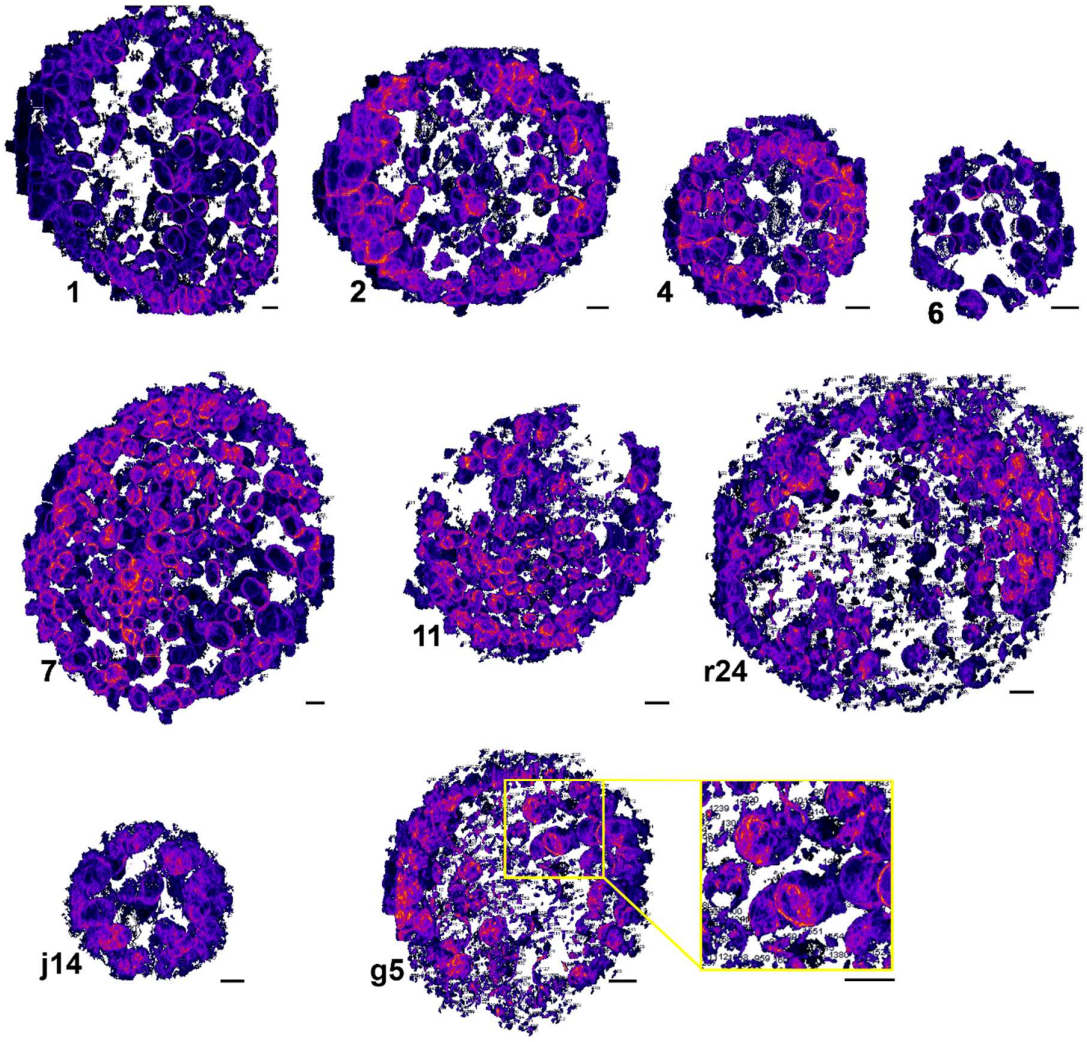

Figure 3: Segmented inclusions after using our pipeline before manual curation. *Inclusions were isolated from the cells using SuRVoS and then bacteria where individually segmented using an ImageJ script. Presented in this figure manually curated data after maximum intensity projection to reveal the volume information. Numbers are generated by ImageJ to identify every volumes. In yellow box a zoom of part of g5. Scale bar: 1 µm*

In order to compensate for the missing wedge, the simulation of spheres of 0.08 μm^3 and 0.3 μm^3 representing the EB and RB respectively (Higashi, 1965) lead us to derive a single correction factor for both sizes (alpha <0.01) (Figure sup 1). Hence, we were able to apply a correction factor to the measured size of the bacteria (which are intrinsically spherical) to correct for the missing wedge data.

Volume calculation and classification of bacteria within the *Chlamydia* inclusion

When considering a population of cells infected by *Chlamydia*, the infection is asynchronous as the size of an inclusion depends on the initial bacterial load which controls both maturation time and volume (Engström, 2015). A population of infected cells was selected judged to be reaching the same 'phase' of infection (Hayward, 2019), such a definition is inherently imprecise for individual cells. In our samples, the inclusions were mostly formed of RBs (non-infectious) with some undergoing transition to EBs (Figure 4 A). This is a complex phase of the life cycle and the signal for the transition is unknown (Elwell, 2016).

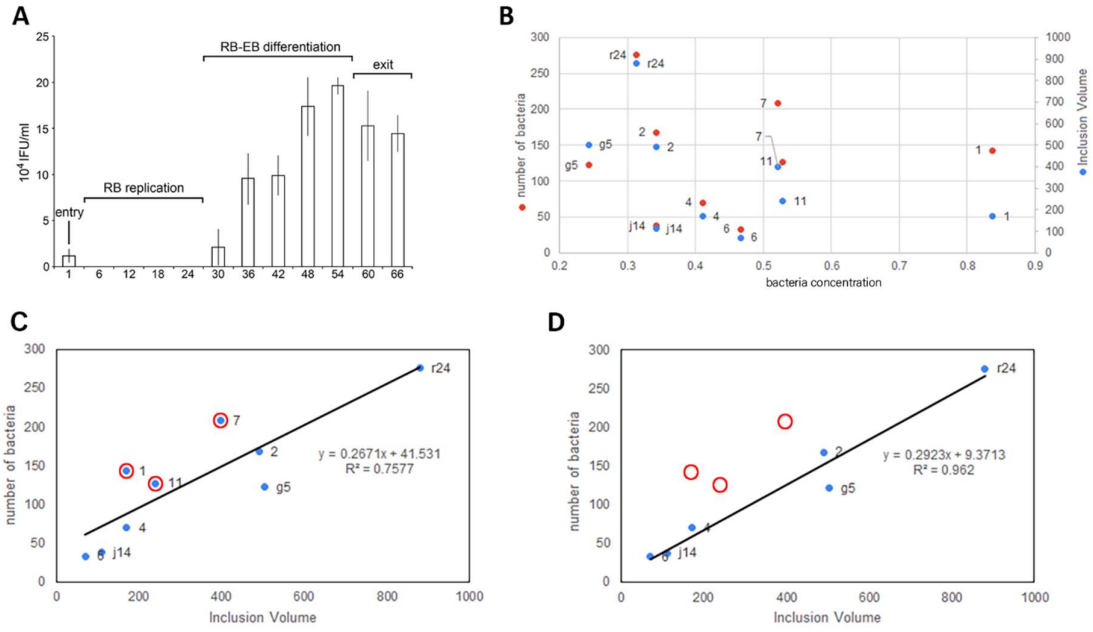

Figure 4: Characterisation of the inclusions included in our dataset. *A) C. trachomatis titration assay in HeLa cells at MOI 0.8. HeLa cells have been infected with C. trachomatis and the cells have been collected at the different time points shown. Then the pelleted infected cells have been used to infect a fresh layer of cells to quantify the inclusion forming units (IFUs). The phase of infection is determined with regards to the IFU. RB: reticulate bodies, EB: elementary body B) After segmentation, each inclusion (ID as a data label in the graph as a number or number plus letter) volume, number of bacteria and consequent bacteria concentration have been plotted. C and D) Number of bacteria as a function of the inclusion volume (C, full dataset D, partial dataset, red circle highlights the absence of inclusion 1, 11 and 7).*

The number of bacteria and the volume of the inclusion are correlated (R^2=0.7577) (Figures 4 B and C) indicating bacterial concentration in the inclusion is a constant **in agreement with Lee et al. (2018)**. However, three inclusions (7, 11 and 1) deviate from this correlation with higher numbers of bacteria per unit volume, removing these three inclusions increases the correlation coefficient for the remaining inclusions (g5 ,r24, j14, 2, 4 and 6) to 0.962 (Figure 4 D). Based on these data, we categorise the inclusions into two broad groups 'standard' (g5 ,r24, j14, 2, 4 and 6) and 'high concentration' inclusions (7, 11 and 1).

Within inclusions, individual bacteria volumes were grouped by increments of 0.05 µm^3. The long standing literature model for *Chlamydia* has EB to be of the order of 0.3 µm in diameter, while RB to be ~1 µm in diameter, persistent bodies (PB) or **aberrant** bodies (AB) to be ~2 µm in diameter and a series of transition bodies (from EB to RB and back, dividing RB, from AB to RB) (Elwell, 2016) (Higashi, 1965) (Matsumoto, 1988). We classified cells by their volume as 'RB', 'EB', 'dividing RB' and 'transition bodies' using volumes derived from the diameter presented in this body of literature. **Transition bodies are bacteria which without a time-resolved approach are difficult to associate to a category as we do not know in which stage and in which direction they are converting to.** The volume of dividing RB was calculated assuming two connected spheres. This method of assignment does not reflect the diversity of the bacterial volumes we observed, for example in inclusion j14, 68% fell outside this classification and therefore have been assigned as abnormally large bodies (Figure 5 and 7).

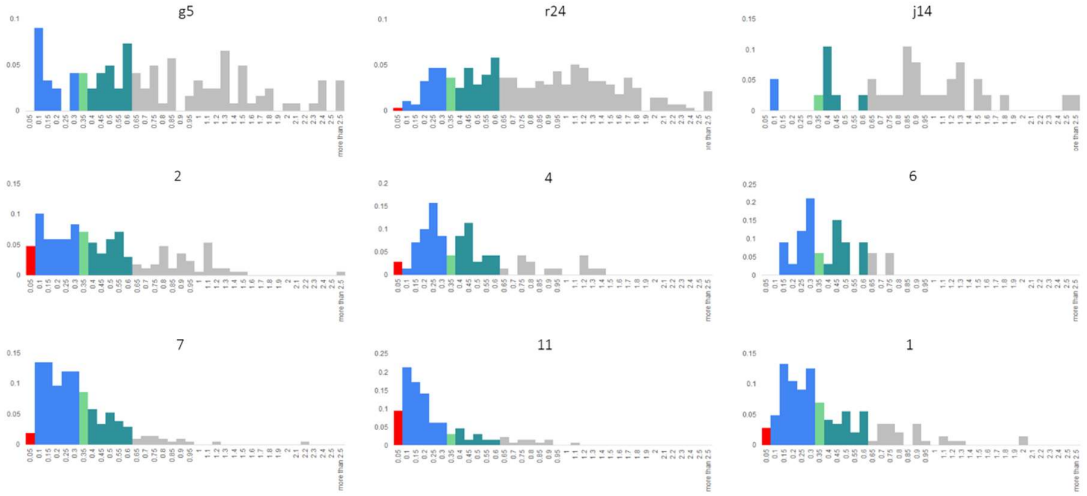

Figure 5: Classification of bacteria population using the most accepted literature criteria to define classes based on volume of the bacteria. *After segmentation, the volume of individual bacteria has been group in classes (x axis) and the percentage of bacteria (events) in each class (colour) is represented on the y axis. Following the literature, red: EB, blue: transition bodies, light green RB, dark green: dividing RB, grey: abnormally large bodies*.

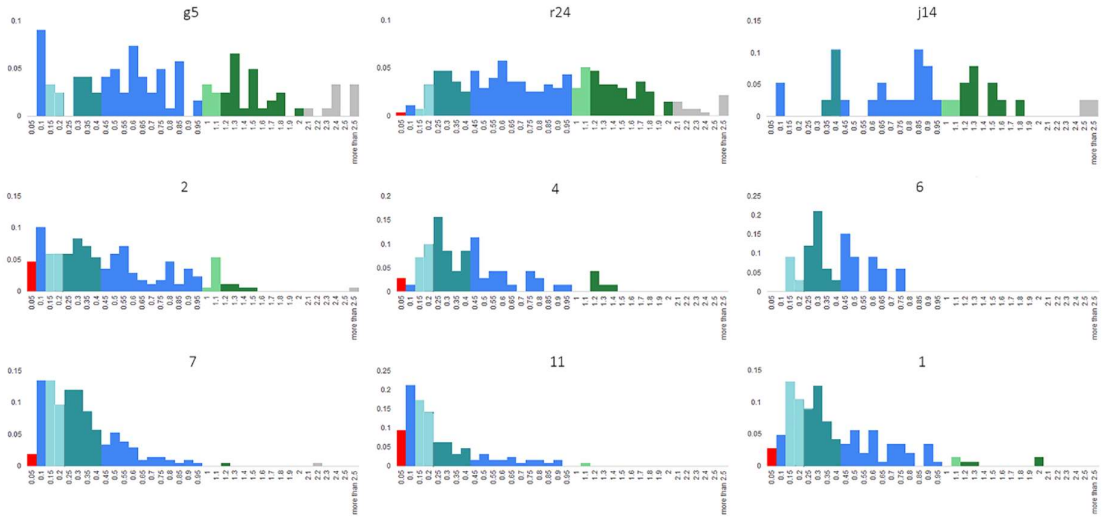

Figure 6: Classification of bacteria population using Lee et al. criteria to define classes based on volume of the bacteria on our dataset *After segmentation, the volume of individual bacteria has been group in classes (x axis) and the percentage of*

bacteria in each class is represented on the y axis. Following Lee and al., red: EB, blue: transition bodies, cyan: small RB, dark cyan: dividing small RB, green: large RB, dark green: dividing large RB, grey: abnormally large bodies.

Lee et al. in 2018 proposed a more complex classification where RB size varied over time from 0.8 μm^3 at 16 hpi, 0.4 μm^3 at 24hpi to 0.2 μm^3 at 32 hpi. The high standard deviation at 24 hpi and 32 hpi (100%) indicated a range were present. Lee et al. report a diameter of 1.25 µm and 0.67 µm for the large and small RB. We used these diameters to divert the volume to apply our pre-set (bacteria b**eing considered** as spheres) and to compensate for the inaccurate volume calculation during sbf-TEM due to artefacts introduced by fixation, staining and sectioning (see introduction)**.** We reclassified bacteria (scenario 2, Figure 6) using the parameters of Lee et al 2018 which added the classes: **'small RB' and 'large RB' and consequently added the derived population 'dividing small RBs', and 'dividing large RB'** (Figure 6, **Methods**). **It has to be noted that in this scenario, the population in blue which represent the transition bodies are present between the EB and RB and between the two different type of RB as bacteria can now transition between three different stages**. In this scenario, at least 92% of the bacterial population was assigned in g5 (Figure 6 and 7) demonstrating the different volumes of RB and associated dividing forms must co-exist to account for the variety of bacterial volumes.

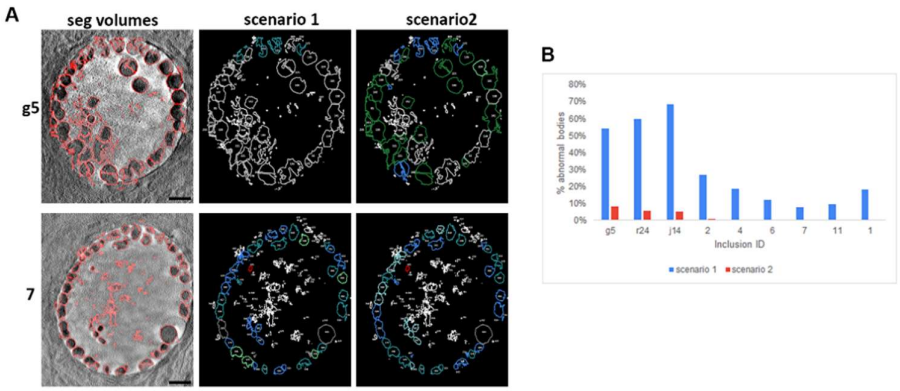

Figure 7: Comparison between the two scenarios a represented in figure 5 and 6. *A) Inclusions (7 and g5) were segmented with the same parameters following scenario 1 or 2. Classification is as followed: red: EB, blue: transition bodies, light green RB, dark green: dividing RB, grey: abnormally large bodies. Scale bar: 5 µm B) number of abnormal bodies per inclusion depending on the parameters used for classification (scenario 1 blue or 2 red).*

Bacteria concentration is not correlated with transition to EB but does correlate with the RB volume

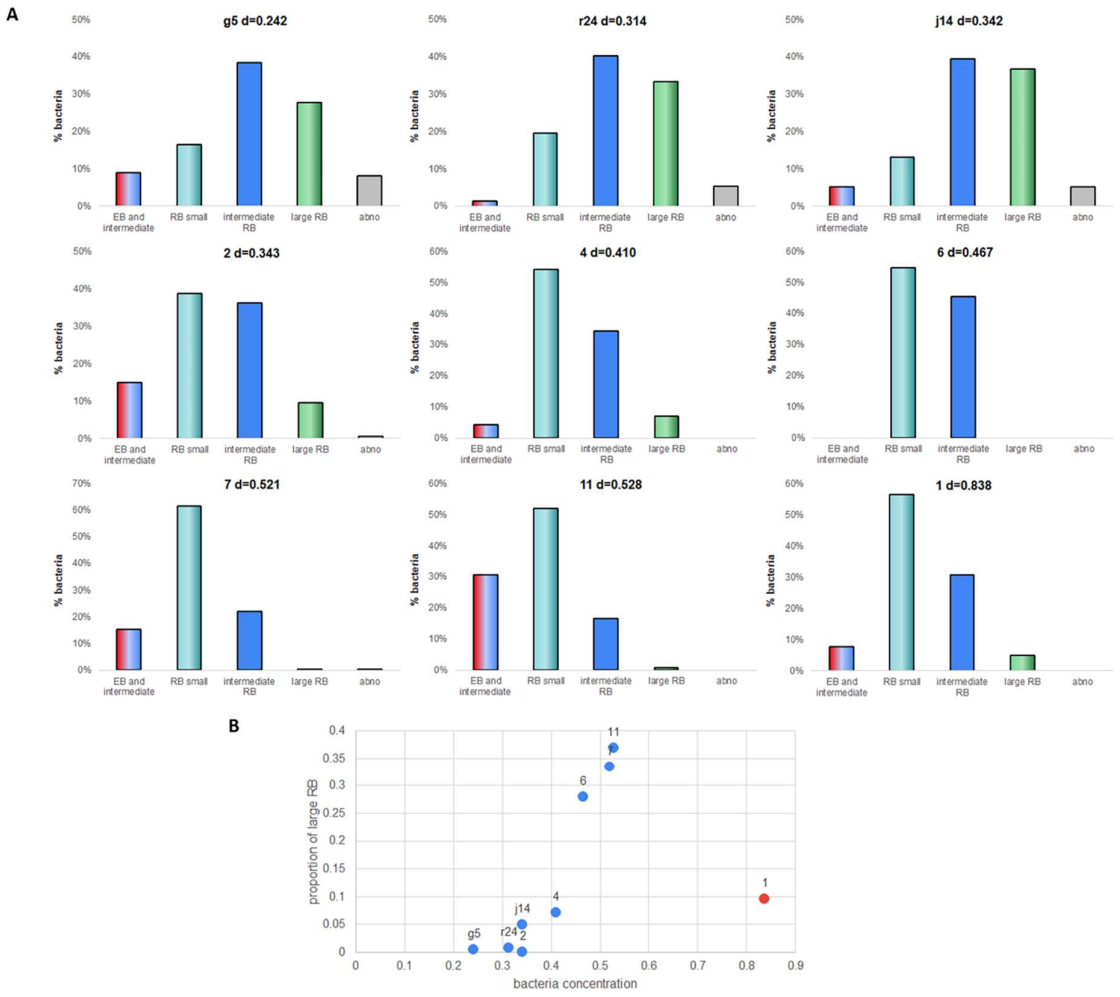

Figure 8: Bacteria classes vary depending on the concentration of bacteria inside the inclusion *A) To ease the analysis the main classes has been represented as a single bar in the histogram as follows: EB and transition: up to 0.1 µm³, small RB at 0.1 to 0. 4µm³, transitioning bodies at 0.4 to 0.95 µm³, large RB at 0.95 to 2 µm³, and abnormal bodies more than 2 µm³.d: density B) Proportion of large RB in function of the concentration of bacteria (bacteria per µm³). In red, inclusion 1 which is outside of the correlation.*

Except for inclusion 11 which had 30% of EB or transitioning bacteria, EBs constituted between 0 and 25% of the total bacterial population. There was no correlation between the proportion of EB and the concentration of bacteria (number per volume) in the inclusions at 24 hpi (Figure 8 A). However, inclusions with the lowest population cell concentration at 24hpi showed an accumulation of large RB and abnormal bodies (Figure 8 A). As the cellular concentration increases, irrespective of the total number of bacteria (Figure 4 to 6), the proportion of abnormally large bodies quickly declines to be absent, the proportion of the large RBs population decreases and the proportion of small RBs increases (Figure 8 A). Overall, at the time where the population of bacteria is at the transition between RB replication and the RB to EB differentiation (Figure 4A), we cannot demonstrate that the transition to EB correlates with the inclusion volume or density. **However, we can demonstrate that the bacteria concentration correlate with the proportion of large RBs (R^2=0.8724) (Figure 8 B) with the again at the exemption of the inclusion 1 which is an very atypical inclusion (Figure 4B)** .

Discussion

Cryo-SXT is a powerful technique allowing the extraction of meaningful metrics from only a few tomograms when the object of interest is present in multiple copies. Reducing the missing wedge of data is highly desirable but needs new approaches to sample presentation, such as using cylindrical sample holders like the national centre for X-ray tomography (Ekman, 2017). However, growing adherent cells and experiments such as transfection, infection or incubation with probes remains challenging for such an approach (Löwe, 2014). Once the data has been collected, segmentation remains a time-consuming bottleneck for data processing, hence we have developed a new workflow to improve the efficiency of segmentation. The ability to collect and analyse datasets in a faster, more automated way, without resorting to population averages, will allow more complex problems to be tackled. Artificial intelligence (AI) and projects based on deep-learning (often with the help of the public) are key for scientists to entirely extract all available information from their samples and datasets (Jones, 2020).

There are two main tomography approaches in biology, electron- or soft X-rays both of which are routinely performed at cryo-temperature to maintain sample integrity. Cryo-electron tomography (cryo-ET) can reach nm resolution and with sub-tomographic averaging atomic resolution (Zhang, 2019) (Tegunov D, 2021) but requires samples thinner than around 120 nm (Egerton, 2015). Serial block face electron microscopy, although not projection tomography, is a powerful approach to visualising 3D volumes, which circumvents the thickness limitation by imaging the surface layer, removing it and imaging the newly exposed surface. This process is however quite slow and requires chemical fixation and heavy metal staining of the cells, all of which generate artefacts. Cryo-SXT can handle much thicker samples (up to 10 µm) and cryo-EM has aided in simplifying sample preparation and expanding the scope of the technique (Duke, 2014). However, the nominal resolution is usually restricted to 35-50 nm (Ekman, 2017). With modification of the zone plate 25 nm can be achieved but this limits the depth of focus to 1 µm (Ekman, 2017).

In order to quickly acquire volume images while working with cryo-preserved thick samples, we used cryo-STX using a 40 nm ZP. We were able to image, segment and characterise bacterial populations within individual *Chlamydia* intracellular inclusions. Imaging with cryo-SXT allows rapid acquisition of a tilt series (completed in 40 mins per area of interest); reconstruction and segmentation taking less than 6-8 hours per tomogram. The open-source workflow for segmentation will allow for further improvements, such as machine learning to be incorporated. Since the technique uses intact cells, it does not require fixation or staining and works at speed so it can be combined with live cell microscopy to observe the evolution of *Chlamydia*. The approach does suffer from distortions introduced due to the missing wedge of data created by the experimental setup and although cylindrical sample holders are known (Ekman, 2017) growing and manipulating adherent cells on them remains challenging (Löwe, 2014)[17]. Nonetheless, *Chlamydia* are mostly spherical object allowing one to derive a correction factor using simulated data so that the volume calculations are not affected by the missing wedge data issue. We have shown that cryo-SXT allows single inclusion imaging which represents important additional functional information. This is because although within each inclusion there is a coordinated community; each individual inclusion develops asynchronously within the cell. Most approaches to imaging *Chlamydia*, have to rely on global averages of infected cells which masks diversity in the individual bacteria communities.

Our imaging data suggest that the proportion of EB within an inclusion are not correlated with the bacterial concentration inside the inclusion. This suggests that the **initial** signal to transition from RB to EB is not a simple nutrient deficiency-based signalling effect but is more consistent with the hypothesis that the RB to EB transition is a multi-factorial event (Chiarelli, 2020)**. However our dataset**

focus on a single time point where the transition to EBs is nascent and we cannot extend our conclusion to later in the life cycle.

The long standing literature model for *Chlamydia* has EB of 0.3 µm in diameter, RB of 1 µm in diameter, persistent bodies (PB) or abnormal bodies (AB) of 2 µm in diameter and a series of transition bodies (from EB to RB and back, dividing RB, from AB to RB) (Elwell, 2016). This model failed to represent the diversity in bacteria we observed for all inclusions, concurring with the conclusions of Lee et al. (Lee, 2018), who using serial block face EM which demonstrated that the RB population is more diverse with a range of volumes. Lee et al proposed that the volume of RB was a function of time, as cells aged, they became smaller. By applying the Lee classification of different sizes, we were largely able to fit the RB diversity we observed at 24 hpi, supporting their categorisation. However, we observed that the proportion of the different RB sizes also varied between inclusions which were all formed at the same time. This would argue against time dependence being the sole factor that determined RB size. Our data show that the RB size was correlated with the bacterial concentration (number of bacteria in an inclusion divided by the inclusion volume) within individual inclusions. Inclusions with low bacterial concentrations showed high proportions of the large RB and a greater number of the even larger abnormal bodies. High bacterial concentration inclusions had a higher proportion of smaller RBs with no or only very few large abnormal bodies. Importantly, inclusions tend to increase the bacterial concentration in time. This would explain the correlation observed by Lee et al. 2018. Engstrom et al. in 2014 demonstrated that the increase in inclusion volume does not require bacterial replication. They observed that inclusions with low bacteria cell concentration accumulated abnormally large bodies, consistent with what we report.

During sbf-EM, the resolution allows the observation of different factors such as the presence of a nucleoid which is characteristic of EBs, allowing for finer and more accurate classification; however, to be able to have a large in-depth volume, and therefore avoid sectioning, the ZP we choose limit our resolution and we are unable to observe such difference. We therefore decided to classify the bodies present between the RBs and the EBs as transition bodies. Regarding the population between dividing small RBs and large RBs (which count for the majority of **transition** body), we intentionally restricted ourselves to an unclassified population. Indeed, we could have had another class of RB corresponding to intermediate size, however, without time-resolved techniques, such as live microscopy and tracking, neither our approach nor sbf-EM can accurately determine the individual bacteria transition between those different states. Additionally, distinctive features, such as protein expressions specific to the different RB forms is still missing. Determining how and when a larger/smaller body are formed and how those different RB transition between each form is a technically challenging question to answer.

Our work has established that cryo-SXT is a useful and very rapid technique to study *Chlamydia*, an important bacterial pathogen. The results we have obtained with this new approach are consistent with more laborious approaches. By being able to focus on individual inclusions within the cell, our data suggest the concentration of *Chlamydia* RB within the inclusion is a very important parameter in determining the range of bacteria morphology. Here we demonstrate **that each inclusion present a different profile of RBs corresponding to a unique set of factors such as the local bacteria concentration**. Future studies along the time domain using this approach will shed light on the evolution of the infection, raise the interest in understanding community sensing (Andrew S. C., 2021) (Prindle A., 2015) and may open new therapeutic opportunities.

Material and Methods

Sample preparation

HeLa cells were grown on 200 F1 grids R2/2 (Quantifoil) one grid per chamber of an 8 well chamber slide (Ibidi). HeLa cells were infected with *C. trachomatis* LGV2 (Dumoux, 2012). At 23 hpi grids were mapped on an Evos FL2 using a 20x objective. At 24 hpi, grids were collected and blotted before addition of 4 µl of fiducials (250 nm silver from Ursa Biosciences) and plunge frozen after a 1 sec back blotting (Leica EM GP).

Soft X-ray tomography

Tilt series were collected on the UltraXRM-S/L220c X-ray microscope (Zeiss, previously Xradia) at beamline B24, Diamond light source with a Pixis 1024 B CCD camera (Princeton instruments) and a 25 or 40 nm zone plate with X-rays of 500 eV. Tilt series were typically collected with an increment of 0.5°.

Tomogram reconstruction

Raw X-ray tomograms were cropped to ensure they had the same tilt ranges and thus the same missing wedge angles. Then, tomograms were reconstructed using eTomo, part of the IMOD package (Kremer, 1996) (https://bio3d.colorado.edu/imod//). The volumes were not filtered before entering the segmentation pipeline. Nonlinear Anisotropic Diffusion (NAD) filtering was used for display purposes.

Simulation data

The simulations were performed at an energy of 500 eV matching the energy used in the experiments at B24 using the attenuation length for Carbon of 331 nm at 500 eV (henke.lbl.gov/optical_constants/atten2.html) using a pixel size of 16 nm mimicking the 40 nm ZP acquisition parameters. For each pixel, i, in the simulated image, the effective thickness of the sample, d_i, was calculated assuming a parallel beam and the intensity for each pixel was then calculated simply as $I_i = I_0 \, exp(-d_i / l)$. In order to avoid pixel artefacts for small spheres sizes, each pixel was sampled in quadrants and then averaged.

Segmentation and classification

For experimental tomograms, a first segmentation was completed using SuRVoS (Luengo, 2017) (https://diamondlightsource.github.io/SuRVoS/docs/installation) to generate a mask to isolate the inclusion from the host cells. This mask was exported and used in ImageJ (Schindelin, 2012) (https://imagej.nih.gov/ij/docs/install/windows.html) to limit the segmentation process to within the inclusion. Simulated data enters the segmentation pipeline at this point. Next, each 2D image was segmented and the volume of each object in pixels cubed was generated using the 3D image counter plugin (S. Bolte, 2006), which also provides a unique identification number for each reconstructed object. The data were then manually curated (Sup Figure 1). The volume of the inclusion was provided by SuRVoS in pixels cubed. All voxels were then converted in micrometre cubed and a correction factor was applied to correct for the missing wedges. Volumes were then classified using 0.05 μm^3 increments. To identify the range of volumes occupied by the bacteria during binary fission, we approximated that the bacteria were perfect spheres which are overlapping and that the minimum distance that could separate them is the resolution limit (40 nm) while the maximum distance is the radius minus the same resolution limit.

References:

Amor, B. (1983). Chlamydia and Reiter's syndrome. *Br J Rheumatol, 4*(2), 156-60.

Andrew S. C., D. M. (2021). Chlamydia Uses K+ Electrical Signalling to Orchestrate Host Sensing, Inter-Bacterial Communication and Differentiation. *Microorganism, 9*(1), 173.

Boland, J. P. (2000). Chlamydia pneumoniae and cardiovascular disease: current status. *W V Med J, 96*(3), 458.

Borel, N. ,. (2018). A Review on Chlamydial Diseases in Animals: Still a Challenge for Pathologists? *Vet Pathol, 55*(3), 374-390.

Cheville, N. F. (2014). Techniques in Electron Microscopy of Animal Tissue. *Veterinary Pathology, 51*(1), 28-41.

Chiarelli, T. J. (2020). Cell Type Development in Chlamydia trachomatis Follows a Program Intrinsic to the Reticulate Body. *under revision mSystems*.

Cottet-Rousselle, C. ,. (2011). Cytometric assessment of mitochondria using fluorescent probes. *Cytometry A, 79*(6), 405-25.

Cunha, B. A. (2006). The atypical pneumonias: clinical diagnosis and importance. *Clin Microbiol Infect, 12*, 12-24.

Davies, D. I. (2006). Actions of ultraviolet light on cellular structures. *Cancer: Cell Structures, Carcinogens and Genomic Instability*, 131-157.

Duke, E. ,. (2014). Biological applications of cryo-soft X-ray tomography. *J Microsc, 255*(2), 65-70.

Dumoux, M. ,. (2012). Chlamydiae assemble a pathogen synapse to hijack the host endoplasmic reticulum. *Traffic, 13*(12), 1612-27.

Egerton, R. F. (2015). Outrun radiation damage with electrons? *Advanced Structural and Chemical Imaging, 1*, 5.

Ekman, A. A. (2017). Mesoscale imaging with cryo-light and X-rays: Larger than molecular machines, smaller than a cell. *Biol Cell, 109*(1), 24-38.

Elwell, C. ,. (2016). Chlamydia cell biology and pathogenesis. *Nat Rev Microbiol, 14*(6), 385-400.

Engström, P. ,. (2015). Expansion of the Chlamydia trachomatis inclusion does not require bacterial replication. *Inter J Med Microbiol, 3*, 378-382.

Gordon, F. B. (1965). Occurrence of Glycogen in Inclusions of the Psittacosis-Lymphogranuloma Venereum-Trachoma Agents. *J Infect Dis, 115*(2), 186-196.

Hayward, M. H. (2019). Early Transcriptional Landscapes of Chlamydia trachomatis-Infected Epithelial Cells at Single Cell Resolution. *Front Cell Infect Microbiol, 9*, 392.

Higashi, N. (1965). Electron microscopic studies on the mode of reproduction of trachoma virus and psittacosis virus in cell cultures. *Exp Mol Pathol, 4*(1), 24-39.

Jolly, A. L. (2019). Stromal Fibroblasts Drive Host Inflammatory Responses ThatAre Dependent onChlamydia trachomatisStrain Type andLikely Influence Disease Outcomes. *mBio, 10*(2), e00225-19.

Jones, F. M. (2020). Processing citizen science- and machine-annotated time-lapse imagery for biologically meaningful metrics. *Sci Data, 7*(1), 102.

Kounatidis, I. ,.-G. (2020). 3D Correlative Cryo-Structured Illumination Fluorescence and Soft X-ray Microscopy Elucidates Reovirus Intracellular Release Pathway. *Cell, 182*(2), 515-530.

Kremer, J. R. (1996). Computer visualization of three-dimensional image data using IMOD. *J Struct Biol, 116*(1), 71-6.

Lee, J. K. (2018). Replication-dependent size reduction precedes differentiation in Chlamydia trachomatis. *nature communications, 9*(45), 1-9.

Löwe, C. M. (2014). A cylindrical specimen holder for electron cryo-tomography. *Ultramicroscopy., 137*(100), 20-29.

Luengo, I. ,. (2017). SuRVoS: Super-Region Volume Segmentation workbench. *J Struct Biol, 198*(1), 43-53.

Matsumoto, A. (1988). Structural characteristics of chlamydial bodies, in: Microbiology of Chlamydia. *CRC Press*, 21-45.

Monikandan, V. J. (2016). Studies on artefacts induced in the specimen preparation. *IOP Conf. Ser.: Mater. Sci. Eng, 149*, 1.

O'Connell, C. M. (2016). Chlamydia trachomatis Genital Infections. *Microb Cell, 3*(9), 390-403.

Prindle A., L. J.-O. (2015). Ion channels enable electrical communication in bacterial communities. *Nature comm., 527*, 59-63.

Radon, J. (1917). Über die Bestimmung von Funktionen durch ihre Integralwerte längs gewisser Mannigfaltigkeiten. *Berichte über die Verhandlungen der Königlich-Sächsischen Akademie der Wissenschaften zu Leipzig, Mathematisch-Physische Klasse* .

Richardson, D. ,. (2007). Lymphogranuloma venereum: an emerging cause of proctitis in men who have sex with men. *Int J STD AIDS, 18*(1), 11-4.

Richter, K. (1994). Cutting artefacts on ultrathin cryosections of biological bulk specimens. *Micron, 25*(4), 297-308.

Robert J. Bastidas, R. H. (2016). Emancipating Chlamydia: Advances in the Genetic Manipulation of a Recalcitrant Intracellular Pathogen. *Microbiol Mol Biol Rev, 80*(2), 411-427.

S. Bolte, F. P. (2006). A guided tour into subcellular colocalization analysis in light microscopy. *J Microscopy, 224*(3), 213-232.

Santarella-Mellwig, R. ,. (2010). The compartmentalized bacteria of the planctomycetes-verrucomicrobia-chlamydiae superphylum have membrane coat-like proteins. *PLoS Biol, 8*(1), e1000281.

Schindelin, J. ,.-C. (2012). Fiji: an open-source platform for biological-image analysis. *Nat Methods, 9*(7), 676-82.

Shelton, S. a. (1978). Membrane blisters: A fixation artifact a study in fixation for scanning electron microscopy. *Scanning, 1*(3), 166-173.

Steven T. Rutherford, B. L. (2012). Bacterial Quorum Sensing: Its Role in Virulence and Possibilities for Its Control. *Cold Spring Harb Perspect Med., 2*(11), a012427.

Taylor, H. R. (2014). Trachoma. *Lancet, 384*(9960), 2142.

Tegunov D, X. L. (2021). Tegunov , D., Xue, L. , Dienemann, C. , Cramer, P., Mahamid, J. *Nat Methods, 18*(2), 186-193.

Waugh, C. A. (2017). Infection with koala retrovirus subgroup B (KoRV-B), but not KoRV-A, is associated with chlamydial disease in free-ranging koalas (Phascolarctos cinereus). *Sci Rep, 7*(1), 134.

Zhang, P. (2019). Advances in cryo-electron tomography and subtomogram averaging and classification. *Curr Opin Struct Biol, 58*, 249-258.